Large-eddy simulations of the flow past a bluff-body with active flow control based on trapped vortex cells at Re = 50000

Dmitry A. Lysenko[a,*], Mark Donskov[a], Ivar S. Ertesvåg[b]

[a]*3DM Simtek AS, Risabergvegen 88, N0–4056, Tananger, Norway*
[b]*Department of Energy and Process Engineering, NTNU Norwegian University of Science and Technology, Kolbjørn Hejes vei 1B, NO–7491, Trondheim, Norway*

Abstract

We investigate a novel flow control concept, which allows to govern bluff-body wake dynamics and the laminar-turbulent transition by suppressing vortex shedding and obtaining the mostly detached flow. Large-eddy simulations past a bluff-body (BB) with and without an active flow control (AFC) system at a Reynolds number of 50000 and zero angle of attack are presented. The BB is designed of a semicircular cylinder of the finite span-wise length with two hemispheres attached to its lateral sides. The BB has a negative lift force because of detached and attached massive recirculation zones, which respectively, originate from separation of the laminar boundary layers from its upper side and the leading edge. AFC is based on the two trapped vortex cells implemented at the upper side of BB to control the behavior of boundary layers. The chosen AFC demonstrates almost the detached flow and suppresses the vortex street. The lift-to-drag ratio of BB with integrated AFC is calculated as ≈ 1.5 (compared to ≈ -1 obtained for the simple BB) coupled with reasonable energy losses of 10% in terms of the total drag coefficient. Finally, present findings demonstrate the potential of the concept and provide the basis for its further development.

Keywords: large-eddy simulation, active flow control, turbulent separated

---

*Corresponding author
Email addresses: `dmitry.lysenko@3dmsimtek.no` (Dmitry A. Lysenko),
`ivar.s.ertesvag@ntnu.no` (Ivar S. Ertesvåg)

flows, trapped vortex cells, bluff body aerodynamics

---

1. Introduction

Active flow control (hereafter AFC) of the flow past different types of bluff-bodies (hereafter BB) is one of the most perspective subjects of discussion in the modern hydro and aerodynamics. Development of advanced vehicles with an improved aerodynamic quality (the lift-to-drag ratio) is ongoing every day, and results provided in this research can be used to form a new technological platform for the next breakthrough of an innovated blended wing-body aircraft with active flow control. Small and medium scale unmanned aerial and autonomous underwater vehicles (UAVs and AUVs) using different passive and active flow control systems is one of the potential areas of the present investigations as well. UAVs and AUVs can be used for a wide range of activities in ocean engineering: transportation, inspection of engineering structures, serving in marine environmental monitoring, observation of the aquatic life, etc. An alternative important area of application in hydro and aerodynamics is the control of bluff-body wakes of structures, and suppression of the related vortex shedding. There is an unlimited amount of examples in ocean engineering and marine science, like vortex-induced vibrations of pipes, bridges, offshore platforms and structures, buildings and city landscapes, etc. For all of these cases the wake control, in principle, can reduce unsteady loads and induced vibrations. It is worth noting that various types of the flow control exist and can be classified into two main groups, namely active and passive, each with their comprehensive overview available in the literature. An outstanding overview of the state-of-the-art methods for the aviation industry was presented by Greenblatt and Williams [1]. Rashidi et al. [2] provided a detailed review of technologies for vortex-shedding suppression and wake-dynamics control. Chen et al. [3] presented results dedicated to the flow control for the circular cylinder. It is interesting to note recent reviews on the bluff-body wakes itself [4],[5].

The present paper will focus on development of AFC (referred as 'active'

according to Rashidi et al. [2]), which is based on the so-called Trapped Vortex Cells (TVC) distributed on the suction (upper) side of the obstacle. According to Sedda et al. [6], the trapped vortex cell is a cavity with a suitably designed shape, which can be mounted on the suction (or/and pressure) side of an airfoil (vehicle) to improve its aerodynamic performances. In the present study, the flow over a simple bluff-body from the semi-circular cylinder of the finite spanwise length, with and without integrated TVCs, is numerically investigated. The AFC system is based on the two trapped vortex cells, interconnected between each other, and the axial circular channel with lateral fluid suction slots (see Figs. 1 and 2). It is shown that the proposed configuration ensures a nearly detached flow past the bluff-body (except the attached recirculation zone from the pressure side and two vortex structures induced from the lateral surfaces of bluff body) with an aerodynamic quality, defined as the lift-to-drag coefficients ratio, of 1.5, as compared to -0.9 obtained for the similar BB without AFC. Reasonable energy losses of 10% in terms of the total drag are achieved, as well. This is in spite of the fact that this configuration is just a preliminary design with some level of abstraction, where the full system of fluid suction from the vehicle engine is replicated by the boundary conditions with the fixed, negative mass flow rates.

Here, we consider appropriate to give a brief genesis of the active flow control systems based on the trapped vortex cells. According to Sedda et al. [6], the idea of trapping vortices was proposed originally by Ringleb [7]. Kasper [8] patented a glider with a trapped structure to observe a high lift. Savitsky et al. [9] exploited the same idea and implemented and tested the 'EKIP', a blended wing-body aircraft equipped with several TVCs.

The next significant milestone can be attributed to the 6th framework EU project called VortexCell2050 (2005-2009). It resulted in a series of experimental and computational works dedicated to fundamental understanding of the concept and related flow physics. A good overview of the activities provided under VortexCell2050 was presented by Sedda et al. [6]. Both experimental and numerical research for the thick airfoils ($40 - 50$% of the chord length) carried

out during years 1995-2005, showed a general possibility to achieve the nearly undetached flow past the thick airfoils with the increased aerodynamic quality and relatively low energy losses charged by the flow control system [10].

The systematic investigation of the thick (37%), MQ1 CIRA and Göttingen airfoils with integrated trapped vortex cells was performed under VortexCell2050 and research projects by Russian Science foundation and Russian foundation for basic research during years 2005-2009. One of the most important result was related to the discovery of the critical Mach numbers, when rearrangement of the flow structures in TVC occurred with the significant drag increase and lift decrease. A good overview and further details of these results can be found in the monograph by Isaev [11].

The present work extends the previous efforts. Here, the bluff body, which is designed as the thick airfoil with thickness of 50% with two integrated TVCs, is investigated using large-eddy simulations (hereafter LES). Numerical calculations are performed for a diameter-based Reynolds number of 50000, Mach number of 0.03 and zero angle of attack. On one hand, this set of parameters (which might not be typical for large-scale vehicles) was chosen to be consistent with our previous studies [12], where the flow around a semi-circular cylinder (hereafter HC) at the Reynolds number Re = 50000 was numerically investigated and will be used as a basis or as a starting point for the further AFC development. On the other hand, it is interesting to compare the present results with experimental and numerical data available for the semi-circular cylinder at Re = 50000 of different span-wise lengths.

There are seven main sections in the paper. The second section explains the concept basis and design. Mathematical modeling and numerical aspects are discussed in the third and forth sections. Subsequently, the computational results are presented, analyzed and discussed, followed by conclusions.

2. Design of the concept

The semi-circular cylinder has drawn attention of researchers due to its low negative lift coefficient ($C_l \approx -1$) at zero angle attack, both from an experimental and a computational point of view [13], [14], [15], [16], [17], [12]. Recently, it was shown [15] that the aerodynamic parameters of this profile can be improved by implementing several trapped vortex cells with slot suction and fluid exhaust into the near-wake flow. However, this problem was computed in two-dimensional space.

The present work utilizes the basic ideas and results by Isaev et al. [15] and extends them to three-dimensional space. Additionally, we leverage our previous results obtained for the flow past a semi-circular cylinder with the different span lengths [12]. Based on the diameter of the semi-circular cylinder and the free-stream velocity, the Reynolds number was set as Re = 50000. The Mach number was set as M = 0.03.

The main design dimensions of BB with and without active flow control system are shown in Fig. 1. The bluff body consists of the main block of the half-cylinder with diameter D and a span length of D, and two attached semi-spherical blocks. The diameter of the half cylinder $D = 0.2$ m is taken as a linear length scale. The total width, height and span lengths of the bluff-body are $BB_x = D$, $BB_z = 0.5 \times D$ and $BB_y = 1.5 \times D$, respectively. BB with active flow control is based on the system of the two trapped vortex cells (TVCs with diameters of $0.2 \times D$ and $0.15 \times D$, respectively) implemented on the suction (upper) side of BB. The span length of both TVCs is equal to D. Both vortex cells are connected by the small channel slots and and the axially directed channel in the half-cylinder body, close to the vortex cells. Left and right surfaces of the radial channel are used for the fluid suction (Fig. 2).

It is worth noting a few additional points: First, the discussed concept was preliminary and used with the purpose to demonstrate the basis of the idea. This design ensures nearly undetached flow past the profile, which is resulting in improvement of the lift force from negative to positive, while maintaining
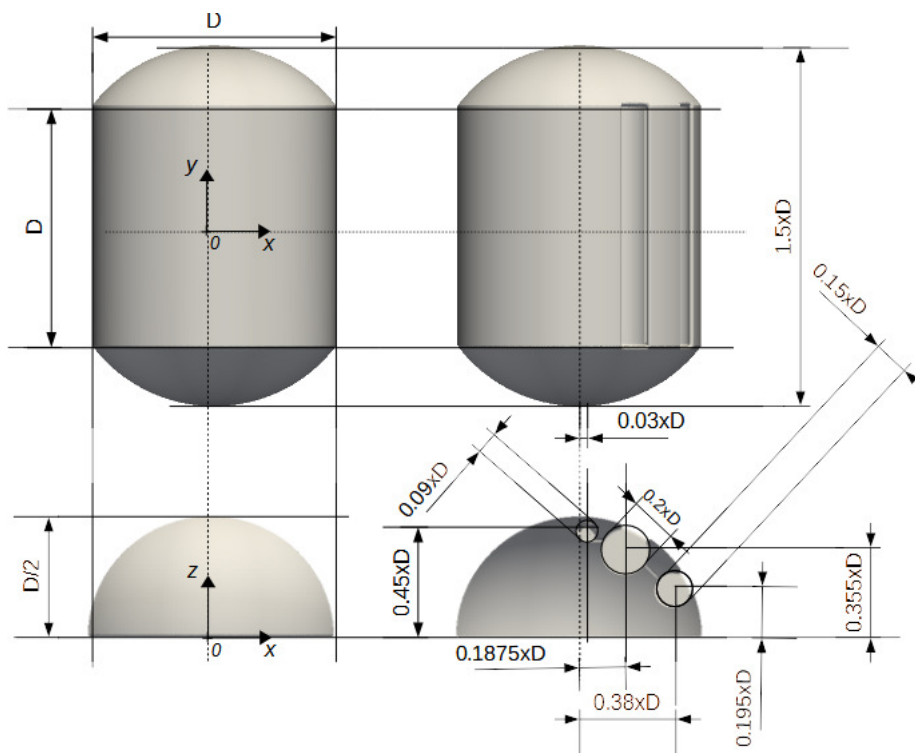
5

Figure 1: Key design features of the bluff-body with and without trapped vortex cells. x, y and z are the domain coordinates in stream-wise, span-wise and transverse directions

approximately the same drag force. Second, this concept has some abstraction of the active flow control system for the fluid suction: the consumed fluid in the present model withdraws inside the bluff-body, which is not realistic in real-life applications. However, authors believe that the present design is satisfactory as a proof-of-concept. Third, as the design starting point, the configurations by Isaev et al. [15] were investigated. The interconnection system between vortex cells and the axially directed channel was obtained after several optimization iterations.
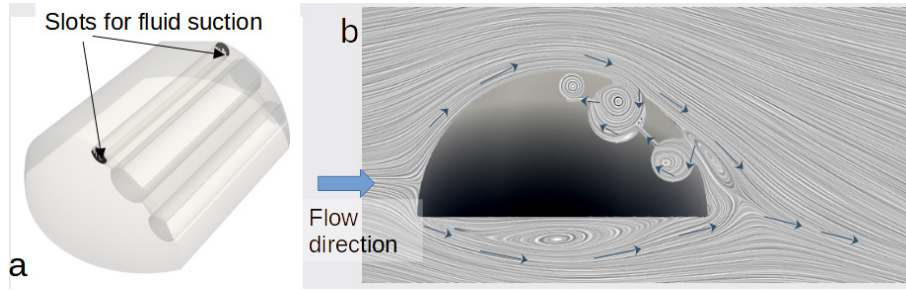

Figure 2: Locations of the surfaces for fluid suction in the active flow control system (a). The flow mechanics over an obstacle with two trapped vortex cells (b)

The physics and topology of the flow over a BB without trapped vortex cells is qualitatively similar to the flow over a semi-circular cylinder with the span length of $10 \times D$, which was discussed in detail in our previous study [12]. Separation of the laminar boundary layers in the subcritical flow regime ($Re = 50000$) provides complex, nonlinear interactions between near and far wakes characterized by the flow instabilities. The Kelvin-Helmholtz instability of the separated shear layer (KH hereafter), as well as vortex shedding (Bénard/von Kármán instability, BVK hereafter), dominate the wake. The developed active flow control system introduces additional recirculation zones and related oscillations in the vortex cells and the axially directed channel. Fig. 2,b displays the schematic flow over the BB with the integrated vortex cells. One can see that operation of the pair of vortex cells prevents the growth of the core of a detached reversed bubble, and rearranges it to relatively small dimensions. The proper superpo-

sition of oscillations for this configuration ensured the nearly undetached flow past the obstacle. The attached separated zone from the pressure side of the obstacle remains unaffected. The flow is stabilized and characterized by a different type of oscillations in the vortex cells, the separated zone attached to the pressure (lower) side and the vortex structures raised from the lateral sides of BB.

The suction and pressure sides of the semi-circular cylinder are defined similarly to airfoils. A detached reversed-bubble recirculation length L_d is defined as the distance between its base and the location for the sign change in the mean stream-wise velocity along the axial direction at $z/D = 0.25$ and $y = 0$.

3. Mathematical modeling

The compressible flow and related numerical setup was considered, even though the actual Mach number was close to the incompressible limit. This was in order to keep consistency with our previous results [18], [19], [20], [21], [12].

The Favre filtered balance equations of mass, momentum and energy were formulated as

$$\frac{\partial \bar{\rho}}{\partial t} + \frac{\partial \bar{\rho} \widetilde{\mathbf{u}}_j}{\partial x_j} = 0, \tag{1}$$

$$\frac{\partial \bar{\rho} \widetilde{\mathbf{u}}_i}{\partial t} + \frac{\partial \bar{\rho} \widetilde{\mathbf{u}}_i \widetilde{\mathbf{u}}_j}{\partial x_j} + \frac{\partial \bar{p}}{\partial x_i} - \frac{\partial \check{\sigma}_{ij}}{\partial x_j} = -\frac{\partial \tau_{ij}}{\partial x_j}, \tag{2}$$

$$\frac{\partial \bar{\rho} \widetilde{h}}{\partial t} + \frac{\partial \bar{\rho} \widetilde{h} \widetilde{\mathbf{u}}_j}{\partial x_j} - \frac{\partial \bar{p}}{\partial t} - \widetilde{\mathbf{u}}_j \frac{\partial \bar{p}}{\partial x_j} + \frac{\partial \check{q}_j}{\partial x_j} - \check{\sigma}_{ji} \widetilde{S}_{ij} = -C_v \frac{\partial Q_j}{\partial x_j}. \tag{3}$$

Density, pressure, and velocity, respectively, are represented by ρ, p, and $\mathbf{u}$. Furthermore, $h = \varepsilon + p/\rho$ represents the enthalpy per unit mass, ε the internal energy per unit mass and T temperature. The marks $(\bar{\cdot})$, $(\widetilde{\cdot})$ and $(\check{\cdot})$ denote the Reynolds-averaging, filtering Favre-averaging and filtering operators, respectively.

The conductive flux and viscous stresses were expressed as

$$\check{q}_j = -\kappa(\widetilde{T}) \frac{\partial \widetilde{T}}{\partial x_i} \tag{4}$$

8

and

$$\check{\sigma}_{ij} = 2\mu(\widetilde{T})\left(\widetilde{S}_{ij} - \frac{1}{3}\delta_{ij}\widetilde{S}_{kk}\right), \tag{5}$$

where $\widetilde{S}_{ij}$ is the rate-of-strain tensor

$$\widetilde{S}_{ij} = \frac{1}{2}\left(\frac{\partial \widetilde{\mathbf{u}}_i}{\partial x_j} + \frac{\partial \widetilde{\mathbf{u}}_j}{\partial x_i}\right). \tag{6}$$

As calculated by Sutherland law, μ represents viscosity, while κ represents conductivity.

For the sake of completeness, a filtered equate of state (EoS) has to be provided in order to close the system of the governing equations. In principle, the present numerical method is quite flexible and allows to model a wide range of fluids using various EoS of the different level of complexity (perfect gas, perfect fluid, real gases, liquids, etc.) without loss of generality. However, the present simulations were performed using the filtered ideal gas equation of state

$$\bar{p} = \bar{\rho}R\widetilde{T}. \tag{7}$$

In this case, the compressible flow is calculated at a Mach number, M $=$ $U_\infty/c_\infty = 0.03$, where U_∞ and c_∞ are the velocity and speed of sound in the free stream, respectively. Due to the low Mach number, the sub-grid scales (hereafter SGS) were assumed to be incompressible [22]. Consequently, the SGS stress τ_{ij} and heat flux Q_j were calculated as follows:

$$\tau_{ij} = \bar{\rho}\left(\widetilde{\mathbf{u}_i\mathbf{u}_j} - \widetilde{\mathbf{u}}_i\widetilde{\mathbf{u}}_j\right), \tag{8}$$

$$Q_j = \bar{\rho}\left(\widetilde{\mathbf{u}_jT} - \widetilde{\mathbf{u}}_j\widetilde{T}\right). \tag{9}$$

For the closure problem, the k-equation eddy viscosity sub-grid scale model [23] was used, based on the SGS kinetic energy, $\tilde{k} = \frac{1}{2}\left(\widetilde{\mathbf{u}\cdot\mathbf{u}} - \widetilde{\mathbf{u}}\cdot\widetilde{\mathbf{u}}\right)$. The SGS turbulence stresses are expressed as

$$\tau_{ij} = -2\mu_B\widetilde{S}_{ij} = -2c_k\bar{\rho}\sqrt{\tilde{k}}\Delta\widetilde{S}_{ij}, \tag{10}$$

with the SGS viscosity computed as

$$\mu_B = c_k\bar{\rho}\sqrt{\tilde{k}}\Delta, \tag{11}$$

9

where a top-hat filter length is Δ. A separately modeled transport equation was used to estimate the sub-grid kinetic energy $\tilde{k}$ of the form,

$$\frac{\partial}{\partial t}\left(\bar{\rho}\tilde{k}\right) + \frac{\partial}{\partial x_j}\left(\bar{\rho}\widetilde{\mathbf{u}}_j\tilde{k}\right) = F_p + F_d - F_\epsilon, \tag{12}$$

where production, F_p, diffusion F_d and dissipation F_ϵ are expressed from

$$F_p = -\mathbf{B} \cdot \widetilde{\mathbf{D}}, \tag{13}$$

$$F_d = \frac{\partial}{\partial x_j}\left((\mu_B + \mu)\frac{\partial \tilde{k}}{\partial x_j}\right), \tag{14}$$

$$F_\epsilon = c_\epsilon \, \bar{\rho} \, \tilde{k}^{3/2}/\Delta, \tag{15}$$

$$\mathbf{B} = \frac{2}{3}\bar{\rho}\tilde{k}\mathbf{I} - 2\mu_B\widetilde{\mathbf{D}}_D, \tag{16}$$

$$\widetilde{\mathbf{D}}_D = \left[\widetilde{\mathbf{D}} - \frac{1}{3}\left(\mathrm{tr}\widetilde{\mathbf{D}}\right)\mathbf{I}\right], \tag{17}$$

$$\widetilde{\mathbf{D}} = \frac{1}{2}\left(\mathrm{grad}\,\widetilde{\mathbf{u}} + \mathrm{grad}\,\widetilde{\mathbf{u}}^{\mathrm{T}}\right). \tag{18}$$

Here, the unit tensor is denoted as $\mathbf{I}$, $\mathbf{B}$ being the density-weighted stress tensor, $\widetilde{\mathbf{D}}_D$ represents the filtered deviatoric part of the rate of strain tensor, and model coefficients are $c_k = 0.07$ and $c_\epsilon = 1.048$ [24].

4. Numerical aspects

4.1. Numerical platform

The numerical platform is based on the finite-volume method of the 2-nd order approximation in space and time and the large-eddy simulation approach with the subgrid scaling model by Yoshizawa [23], implemented in the Open-FOAM toolbox [25]. The platform has proven to be an efficient and accurate tool for investigating external hydro and aerodynamic problems and turbulent flows in the last decade [18], [19], [26], [27], [28], [29], [20], [30], [31], [21], [12].

The OpenFoam toolbox is based on a set of libraries to solve systems of partial differential equations (PDEs) implemented using the C++ language. By manipulating of the C++ semantics, the code provides a human-readable

form for most mathematical differential and tensor operators, allowing to completely encapsulate and isolate several concepts: computational grid (discretization method), approximation of the governing PDEs and methods to solve systems of the linear algebraic equations [25]. Finally, the toolbox is accompanied by a set of applications, where various mathematical models of the continuum mechanics are implemented.

The specifications of the platform for high performance computing to solve the turbulent separated flows were investigated in our previous studies [32], [12]. For up to 1024 cores, a reasonable good strong and week scaling was demonstrated with an average efficiency of about 70%. As compared to competing implicit pressure-based solvers implemented in the commercial CFD (computational fluid dynamics) codes, these results were quite satisfactory for the state-of-the-art implicit pressure-based solvers.

OpenFOAM v6.0 was used for the simulations. For solving the governing equations, the PISO (pressure implicit with splitting of operators) method [33] and the standard pressure–velocity coupling methodology were used, followed by the PIMPLE algorithm [28]. All dependent variables except pressure were solved using a smooth solver (with a symmetrical Gauss-Seidel smoother) with a local accuracy of 10^{-7}. A geometric agglomerated algebraic multigrid solver (GAMG) and a Gauss-Seidel smoother were used to compute the system of linear algebraic equations. To avoid artificial pressure oscillations, the LUST (Linear-Upwind Stabilized Transport) divergence scheme [34] was used with 0.25 linear-upwind and 0.75 linear weights. In addition, the total variation diminishing (TVD) scheme [35] was used to approximate all other terms. Time integration was performed by applying the 2-nd order scheme (backward differential formula, BDF-2 [22]) with a dynamic time stepping technique to maintain a Courant number below 0.4.

4.2. Boundary and initial conditions

The Reynolds and Mach numbers were set by specifying the free-stream inflow velocity, temperature, and turbulence properties. Using the ideal gas law,

11

the fluid medium was treated as compressible air (with $\phi = 1.4$ as the specific heats ratio). A Prandtl number of 0.72 was used and its assumed constant values for the dynamic viscosity and thermal conductivity. In order to provide computational stability for LES calculations, the inlet value for the turbulence intensity was set to 0.2%. All inflow boundaries were imposed with a zero-gradient for pressure, while the outlet pressure was set at 101325 Pa. The surface of the vehicle was treated with a non-slipping condition for velocity under the hydrodynamically smooth assumption. At the surface of the bluff-body, the turbulence kinetic energy was zero. At the lateral boundaries, symmetry planes were imposed. The zero-gradient assumption was used to determine boundary conditions for temperature at solid walls. A negative mass flow rate ($Q_m = 0.016$ kg/s) was imposed at each of the fluid suction slots. The initial conditions were based on the inflow conditions.

4.3. Computational domain and grids

The center of the Cartesian x, y, z, coordinates was located in the center of the BB base and specified in Fig. 1. Several grids were used for the present LES.

The computational domain of the first grid had dimensions of $25D \times 25D \times 25D$ in x, y and z directions, respectively (Fig. 3,a). Three grids were designed for the bluff-body without the trapped vortex cells and two grids for the obstacle with AFC. Hereafter, the following tags are assigned for these grids: BB01, BB02 and BB03 (without TVC) and AFC01 and AFC02 (with TVC). Initially, the computational box consisted of $25 \times 25 \times 25$ nodes. Then, the grids were sequentially refined up to five levels with a factor of $2 \times 2 \times 2$. Table 1 provides basic information like the refinement areas with the related cell sizes and the associated mesh tags. Note that the AFC02 grid was designed in the similar way, but with the different cell sizes. Fig. 3 displays some insight to the designed meshes. The viscous boundary layer of three levels was attached to the obstacle in all grids. Finally, Table 2 gives the total number of control volumes for the each grid and computed, averaged non-dimensional distance to the wall, $\bar{y}*$, for
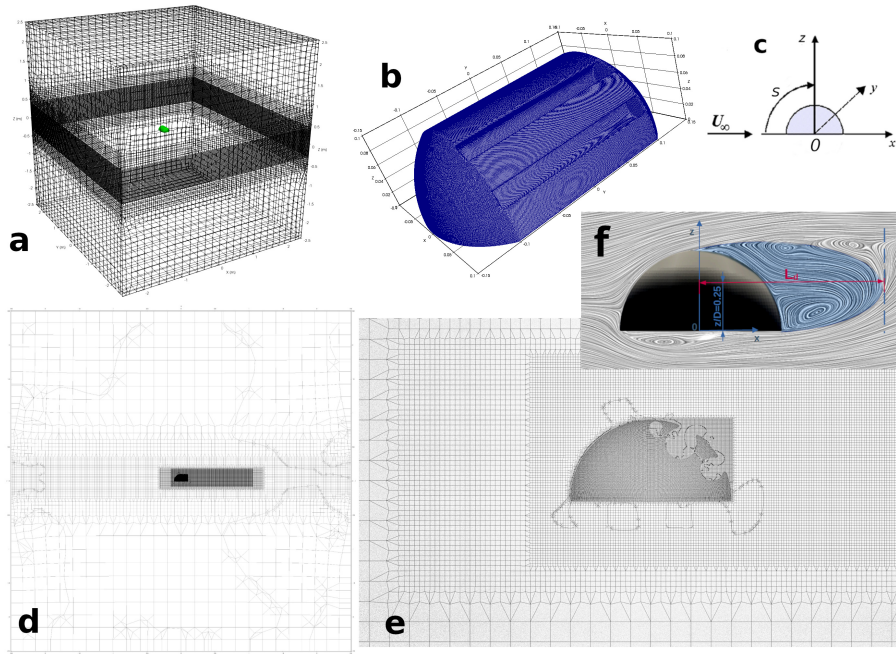
Figure 3: General view of the computational domain (a), bluff-body with the active flow control system (b), description of the AFC02 grid in the central $x - z$ plane (d), zoom of this grid at the vicinity of the bluff-body (e). x, y and z are the domain coordinates in stream-wise, span-wise and transverse directions. Definition of the recirculation zone length for BB, L_d (f). s is the circumferential coordinate (c), normalized by the total length of the semi-circular profile $(\pi D/2 + D)$

13

the nearest cell.

Table 1: Overview of the designed grids in the matrix form to compare them in terms of the refinement levels: Level adaptation (L), cell size (Nc), refinement Box (lengths in x, y, z), and its Center and the associated grid tags. All linear scales are dimensionless by D

L	Nc	Box	C	BB01	BB02	BB03	AFC01	AFC02(Nc)
0	1.0	[25, 25, 25]	[0.000,0.0,0.000]	+	+	+	+	+
1	0.5	[25, 25, 5]	[0.000,0.0,0.000]	+	+	+	+	+(0.4)
2	0.25	[25, 25, 2.5]	[0.000,0.0,0.000]	+	+	+	+	+(0.2)
3	0.05	[7.5, 2.5, 1.5]	[2.250,0.0, 0.250]	+	+	+	+	+(0.04)
4	0.025	[6, 2.25, 1.25]	[2.250, 0.0,0.250]		+	+	+	+(0.02)
5	0.0125	[2, 2, 1.05]	[0.375,0.0, 0.175]			+	+	+(0.00375)

Table 2: Total grid size (S) in millions and averaged non-dimensional distance to the wall $\bar{y}*$

	BB01	BB02	BB03	AFC01	AFC02
S	2.9	7.9	14.8	8.9	23.2
$\bar{y}*$	0.65	0.73	0.72	7.47	5.84

It should be noted that the following span resolutions (Δz) were utilized in the present study: $\Delta z/D = 0.025$ (BB02) and $\Delta z/D = 0.0125$ (BB03, AFC01, AFC02). There are few studies in the literature that allow to assess the span resolution. Williamson et al. [36] suggested the scaling for the span-wise wave lengths as $\lambda/D \approx 0.1$ or $\lambda/D \approx 25/\sqrt{\mathrm{Re}}$ at Re $= \mathcal{O}(10^4)$. Cao et al. [37] provided a detailed study of the span resolution requirements for the flow over a square cylinder at Re $= 22000$ and recommended $\Delta z/D \leq 0.02$ to predict accurately the shear layer behaviors and the laminar-turbulent transitional process. Lysenko et al. [12] investigated the flow over a semi-circular cylinder at Re $= 50000$ and found these estimations quite suitable. In the present study, all the fine-resolved grids (BB03, AFC01, AFC02) satisfied the stringent requirement by Cao et al. [37], $\Delta z/D \leq 0.02$.

A conventional approach for pragmatic LES [38] to assess the turbulence length scales and required grid resolution is to estimate the Taylor $\lambda_T^2 = 10\nu K/\epsilon$
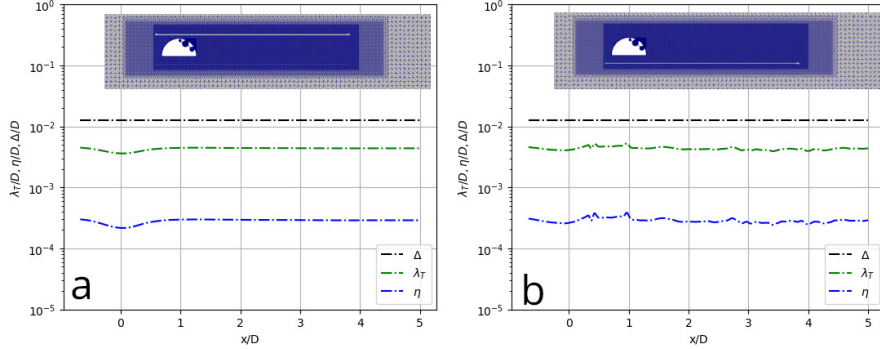
Figure 4: Comparison of axial distributions of the sub-grid filter (Δ) and instantaneous Taylor (λ_T) and Kolmogorov scales (η) for the AFC01 grid: a – $z/D = 0.625$, $y/D = 0$ and b – $z/D = -0.25$, $y/D = 0$ (marked as the white lines at the top of the each sub-figure)

and Kolmogorov scales $\eta = (\nu^3/\epsilon)^{(1/4)}$, where ν is the kinematic viscosity, K is the mean turbulence energy (i.e. entire spectrum), and ϵ its dissipation rate estimated from Eq. 15. Figure 4 displays axial distributions of the sub-grid filter and the instantaneous Taylor and Kolmogorov scales at the two axial states calculated for the AFC01 grid. Quite obviously, the Kolmogorov scales were located more than a decade lower than Taylor scales and the sub-grid filter scale was the same order as Taylor micro-scales, which demonstrate that the present LES grids guarantee an adequate resolution of the turbulence length scales.

4.4. Grid dependence study

Figure 5 shows the most important integral parameters for assessing the grid convergence: the mean drag coefficient $\langle C_d \rangle$ and mean recirculation zone length $\langle L_d/D \rangle$ in the same spirit as [21]. Here, the recirculation length L_d is defined as in Sect. 2 for the BB cases (Fig. 3,f). When $z/D = 0.05$ and $y = 0$, the recirculation length of the detached bubble L_{da} for AFC runs is defined as the distance between the base of the cylinder and the location of the sign change of the mean stream-wise velocity.

It was evident that a deviation for the mean drag as a function of the cell

15

number was bounded by ±2% both for BB and AFC runs. The largest discrepancy of ±6% was found for the length of the detached bubble formed during operation of the trapped vortex cells. However, these length scales are relatively small compared to the primary recirculation zones of the BB cases, and the observed deviation could be reasonably accepted in the present study.
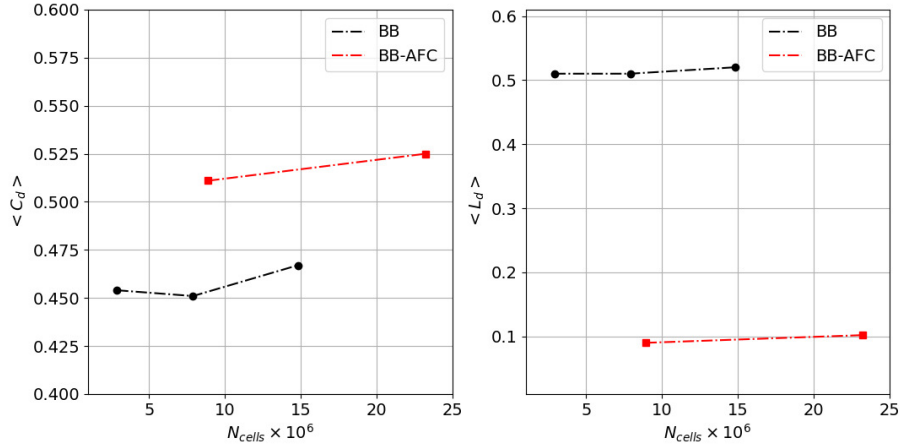

Figure 5: Dependence of the mean drag coefficient (a) and mean recirculation zone length (b) on the grid size

5. Results

5.1. Overview

The solution was initiated from fluid at rest. After one flow-through time, the solution was considered statistically convergent. In this study, the flow-through time was defined as the ratio between the axial length of the computational domain and the bulk velocity. After the flow field was converged, one more flow-through time was sampled for data analysis.

The time-averaging operator is denoted by $\langle \rangle$. Simulated cases were BB01, BB02, AFC01 and AFC02 using the meshes according to Tables 1 and 2. All runs were carried out at the fixed Reynolds and Mach numbers, $\mathrm{Re} = 50000$ and $\mathrm{M} = 0.03$.

This section is divided into two parts. First, it is interesting to compare results between the present BB and HC of the finite span length $(10 \times D)$, which was computed using a similar numerical approach [12]. Then, effects of the trapped vortex cells are discussed comparing results between BB and BB-AFC. The primary difference between the HC and BB cases were the span lengths and the shapes of the body ends.

5.2. The obstacle without active flow control system

5.2.1. Mean flow features

A summary of the main integral flow parameters is given in Table 3, including the lift C_l, drag C_d, pressure base C_{pb} coefficients and Strouhal number St_p. For quantitative comparison and analysis, the detached recirculation zone L_d was also added.

Table 3: A set of integral flow parameters derived from experimental (EXP) and numerical results (NUM; i.e. LES with an SGS turbulence energy equation, Sect. 3) for the flow past the semi-circular cylinder and bluff-bodies with and without integrated trapped vortex cells at Re $= 40000 - 50000$

Contributors	Method	Grid size	L_y/D	$\langle C_d \rangle$	$\langle C_l \rangle$	$-\langle C_{pb} \rangle$	St_p	$\langle L_d \rangle$
Sluchanovskaya [13]	EXP		16	0.5	-1.1	0.62		
Yamagata et al. [14]	EXP		12.7	0.37	-0.54		0.37	
Isaev et al. [16]	EXP		16	0.467	-0.634	0.96	0.41	
Isaev et al. [16]	EXP		4	0.476	-0.816	0.98	0.44	
Lysenko et al. [12] HC1	NUM	11M	10	0.529	-0.986	0.62	0.396	0.86
Lysenko et al. [12] HC2	NUM	25M	10	0.468	-1.055	0.54	0.371	0.86
Present: BB02	NUM	7.9M	3	0.451	-0.434	0.51	0.321	0.51
Present: BB03	NUM	14.8M	3	0.467	-0.427	0.53	0.327	0.52
Present: AFC01	NUM	8.9M	3	0.511	0.749			0.09
Present: AFC02	NUM	23.2M	3	0.525	0.760			0.102

Distributions of the mean pressure coefficient, $\langle C_p \rangle$, and normalized vorticity, $\langle \Omega \rangle$, over the bluff-body, obtained in the central $x-z$ plane $(y = 0)$ are plotted in Fig. 6. The mean pressure coefficient is defined as $\langle C_p \rangle = 2(\langle p \rangle - p_\infty)/(\rho_\infty U_\infty^2)$, where p_∞, ρ_∞ and U_∞ are free stream pressure, density and velocity, respectively. The computed $\langle C_p \rangle$ satisfactorily replicated experimental data by Sluchanovskaya [13] and the previous results (HC1 and HC2 runs [12]) on the

suction side of the profile. It can be seen that numerical results obtained using the low and high resolution grids were relatively well collapsed. Furthermore, there was reasonable agreement of the present results for HC1 and HC2 with estimated experimental data by Son and Hanratty [39] for the normalized vorticity at the suction side.

The further mismatch in $\langle C_p \rangle$ and $\langle \Omega \rangle$ observed at the pressure side of the bluff-body was due to different flow patterns computed in the present and previous (HC1 and HC2) LES calculations (Fig. 7). One can see that the topology of the flow at the suction side was quite different between the HC and BB cases, Fig. 7a, and Fig. 7,b, respectively. The HC recirculation zone consisted of the major core and two counter-rotating vortices attached to its suction size, which propagated approximately from the leading edge to the trailing edge. The separation zone attached to the pressure side of the BB covered approximately half of the the pressure side and vanished towards the trailing edge of the HC. A satisfactory agreement was found between the present $\langle C_p \rangle$ and Sluchanovskaya's measurements [13]. The mean normalized vorticity $\langle \Omega \rangle$ was reasonably matched to experimental results by Son and Hanratty [39] for the circular cylinder (hereafter CC) at Re = 20000 and Re = 50000.

Evidently, the stagnation point ($s = 0$) for HC and BB was moved up along the upper side to approximately $s = 0.06$ (Fig. 6). At this point, $\langle \Omega \rangle$ was vanishing mostly to zero. According to the flow separation angle θ at the suction side of HC, the stagnation point can be identified. Here, θ was defined as the angular coordinate starting from the leading edge. Previous LES results (HC1, HC2) for $\langle \Omega \rangle$ presented in Fig. 6 collapsed well with experimental results [39] up to $\theta \approx 90°$. However, the present LES results (BB02 and BB03) matched HC1, HC2 and measurements up to $\theta \approx 80°$, indicating that the separation point of boundary layers was slightly shifted upstream to the leading edge. According to the analytical solution from the boundary layer theory and measurements [39], the separation for CC should occur at $\theta = 78°$ for this Reynolds number. Interestingly, our previous LES results for CC [19], where $\theta \approx 86° - 88°$ was obtained, were consistent with the present calculations.
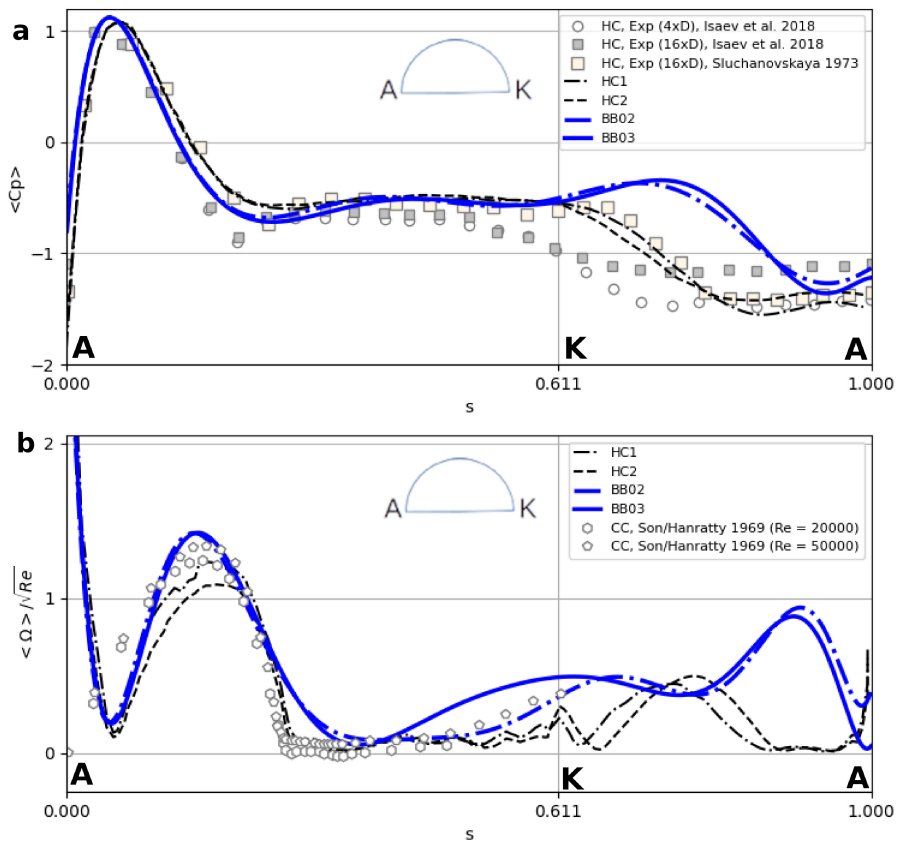
18

Figure 6: Mean pressure coefficient (a) and normalized vorticity (b) along the circumferential coordinate, s (see Fig. 3,c), for the flow over HC and BB at Re $= 50000$

Variations in predictions of the separation angle between the present results and those reported earlier for the circular [19] and semi-circular [12] cylinders could be explained by the finite length effects in the span-wise direction. In practice, all currently examined bluff-bodies have the finite span length compared to the obstacles of the infinite span length (in theory) from the previous works. The finite/infinite span length gap leads to the different flow patterns over the obstacles, as well as separated zones attached to them (pronounced in Fig. 7 clearly), which are characterized by a slight dispersion in the laminar/turbulent transition and boundary layer separation. However, numerical effects should be considered as well.

The value of $\langle C_p \rangle$ on the obstacle surface at the trailing edge can be defined as the base suction coefficient $\langle C_{pb} \rangle$. The calculated values $-\langle C_{pb} \rangle = 0.51 - 0.53$ correlated well with the results obtained for HC1, HC2 ($-\langle C_{pb} \rangle = 0.54 - 0.62$) and with the experimental value by Sluchanovskaya [13], $-\langle C_{pb} \rangle = 0.62$. According to Isaev et al. [16], the mean base suction coefficient, $-\langle C_{pb} \rangle = 0.96 - 0.97$, was significantly different (by 36%).

The drag and lift coefficients C_d and C_l were integrated using the pressure at the surface of the semi-circular cylinder. The cross-sectional area of the vehicle was used as the reference area to calculate the coefficients. In agreement with the HC results ($\langle C_d \rangle = 0.468 - 0.529$), and the experimental results by Sluchanovskaya [13] and Isaev et al. [16], the mean drag coefficient was calculated to be $\langle C_d \rangle = 0.451 - 0.467$.

Table 3 summarizes the total drag coefficient including both the viscous and pressure contributions. One can see that the Strouhal number was quite sensitive to the dimensional effects. It is important to note that surface roughness effects can introduce some impact to deviations between the physical experiments and numerical results. The present numerical analysis was carried out using the so called 'hydrodynamically smooth' assumption for all BB surfaces. In practice, any meaningful numbers for the average roughness (Ra) for the experimental obstacles ([13], [14], [16]) were not provided. As a conservative approach, the surface roughness, Ra ~ 0.5 μm could be considered. The calcu-
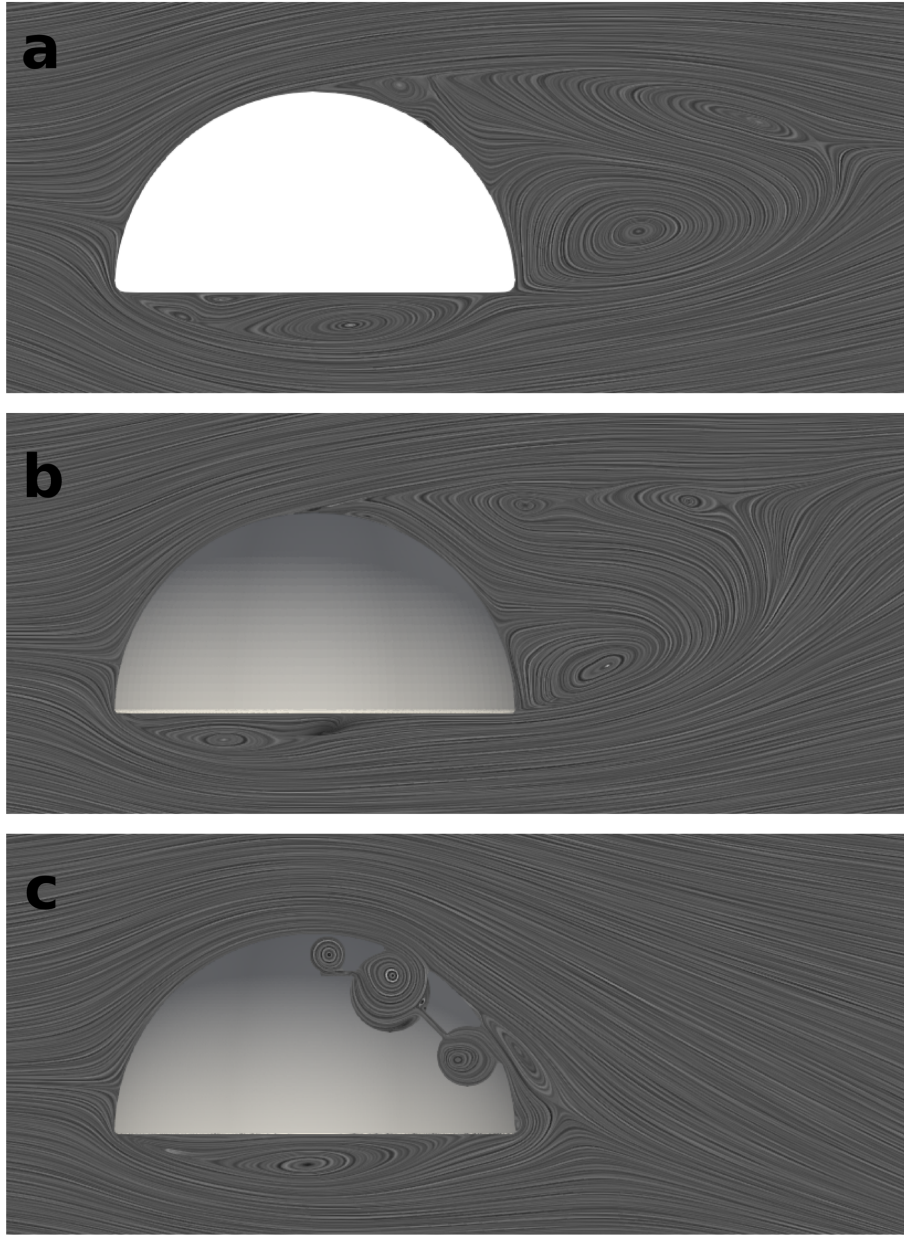
Figure 7: Time-averaged streamlines for the flow over a semi-circular cylinder, HC2 run from Lysenko et al. [12](a), present LES for the bluff-body without the trapped vortex cells (b) and with active flow control (c) at Re = 50000 computed in the $x - z$ plane at the middle of the span length $(y = 0)$

lated minimum viscous length scale (the ratio between the kinematic molecular viscosity and the frictional velocity) for the flow conditions was, $\sim 15\ \mu$m, which was the two order of magnitude larger than the assumed experimental Ra, and thus no significant impact on the drag force should be expected [40].

For HC1 and HC2, a negative mean lift coefficient of $-\langle C_l \rangle = 0.986 - 1.055$ was obtained. It was found that these values were in good agreement with the experimental data by Sluchanovskaya [13], who measured $-\langle C_l \rangle = 1.1$. They were also significantly over-predicted by Isaev et al. [16], who measured $-\langle C_l \rangle = 0.634 - 0.816$. The present LES predicted the lift coefficient as $-\langle C_l \rangle = 0.434 - 0.427$. This was approximately two times above HC and experimental results by Sluchanovskaya [13], and can be explained by effects introduced by the BB shape with the two semi-spheres integrated from the left and right sides of BB.

The computed recirculation lengths of the detached separated zones at the suction side of the obstacle were $\langle L_d \rangle = 0.51 - 0.52$, approximately 40% shorter than the computed vales for HC1 and HC2 ($\langle L_d \rangle = 0.86$). The difference in the detached separation zones between the present results and HC1, HC2 are shown in Fig. 7,a,b. These deviations can be explained the superposition and interaction between the prime detached bubble and two horseshoe-type vortical structures, generated by the BB semi-spheres.

5.2.2. First and second order statistics

The mean stream-wise velocity $\langle U \rangle / U_\infty$ along the center line is presented in Fig. 8,a. For qualitative assessment, we analyzed our previous LES results (HC1, HC2) [12]. Furthermore, experimental and numerical results were accumulated for circular ([41], [42], CC hereafter) and square ([43],[44], [45], [46], [47], SC hereafter) cylinders.

The main difference between the present LES results and data plotted in Fig. 8 is in recovering of both $\langle U \rangle$ and $\langle U'U' \rangle$ to its free stream values. The minimum values of the mean stream-wise velocity, $\langle U \rangle / U_\infty$, were found to be similar to those of HC1, HC2 (-0.18 to -0.2). This was close to the experimental data
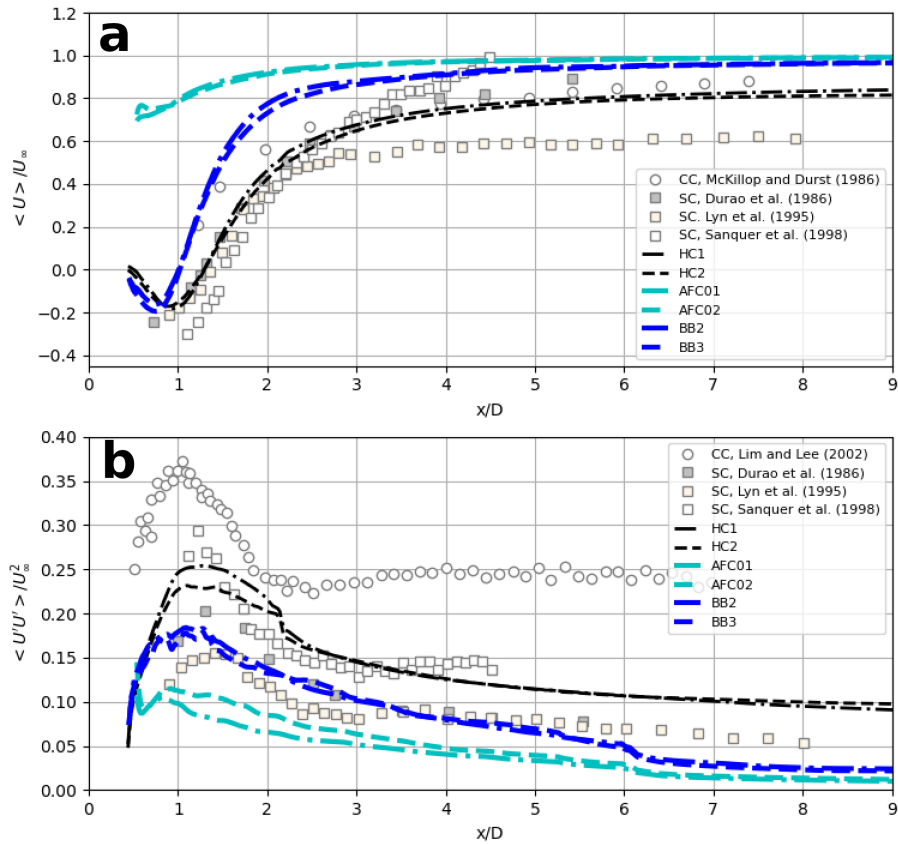
Figure 8: Profiles of the mean stream-wise velocity, $\langle U \rangle / U_\infty$ (a), and normal stresses, $\langle U'U' \rangle / U_\infty^2$ (b), in the wake centerline in the middle of the span ($y = 0$) for the flow over BB and BB-AFC at $\mathrm{Re} = 50000$. Experiments for circular (CC) and square (SC) cylinders

by Durao et al. [43], McKillop and Durst [41], Lyn et al. [44] and Trias et al. [47]. In practice, Durao et al. [43] and McKillop and Durst [41] obtained similar experimental trends in their measurements. Figure 8,b shows the profiles of the mean normal stress, $\langle U'U' \rangle / U_\infty^2$, along the centerline. It is noteworthy that CC and SC have large gaps in mean normal stresses. Data from CC and SC showed more than twice different peak values of the normal stresses, which corresponded to the primary separation bubble. The present LES curves trended to be less than the results by HC1, HC2, but were close to data by Durao et al. [43] and Sanquer et al. [45] for SC.

5.2.3. Spectral analysis

As shown in Figs. 9,a,b, vortex streets were formed downstream of HC and BB, as well as the coherent flow structures, demonstrated by the Q-criterion, $Q = S^2 - \Omega^2 = 10^4$, where S is the strain rate and Ω is the vorticity. The visualization of the turbulent wake showed the capability of the present simulations to resolve a wide range of the vortex structures. The vortex cores were clearly identified on the pressure and suction sides of the obstacle surfaces during the separation of the laminar boundary layers (the 'sub-critical flow regime'). As the vortex cores formed, the mean flow convected them further downstream.

In the post-shear-layer transition, the vortex shedding instability had a characteristic frequency of $f_{vs} = \text{St}_p U_\infty / D$, where St_p is the Strouhal number. Figure 10 illustrates the resulting characteristic frequencies of the vortex shedding instability computed from the velocity signals sampled at several probe locations near the bluff-body at $x/D = 1, z/D = 0$ and $x/D = 1, z/D = 0.25$. For increased statistical power, spectra were averaged in the span-wise direction (11 uniformly distributed probe locations were used). The Welch periodograms [48] and fast Fourier transforms (FFT) were used to compute the one-dimensional spectra. The frequency was nondimensionalized by the Strouhal shedding frequency (f_{vs}). The experimental results of Ong and Wallace [49] and Parnaudeau et al. [50], and a $-5/3$ slope are depicted, as well. By reproducing the inertial sub-range clearly over a wide spectral range, the present LES provided the not
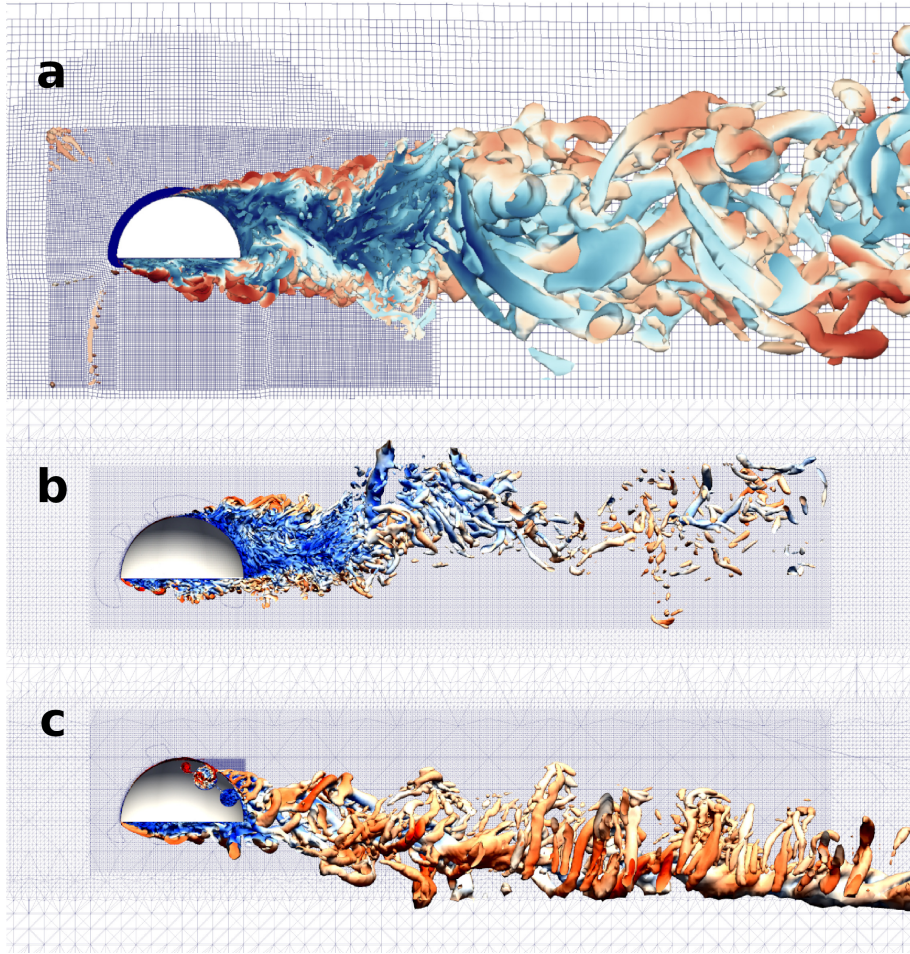
Figure 9: Visualization of flow structures obtained for the flow past a semi-circular cylinder (HC2, a), bluff-body without trapped vortex cells (BB02, b) and with integrated active control system (AFC02, c). Iso-surfaces of the Q-criterion ($Q = S^2 - \Omega^2 = 10^4$, where S is the strain rate and Ω is the vorticity)

over-dissipative SGS modeling. The physical sense of the results portrayed in Fig. 10 suggests an ability of the present simulations to resolve a wide range of the coherent, energetic flow structures (supported by the visualization in Fig. 9). Also, one can see clearly that the spectral distribution of these energy scales obeys to the fundamental -5/3 law, intrinsic to the turbulent flows.
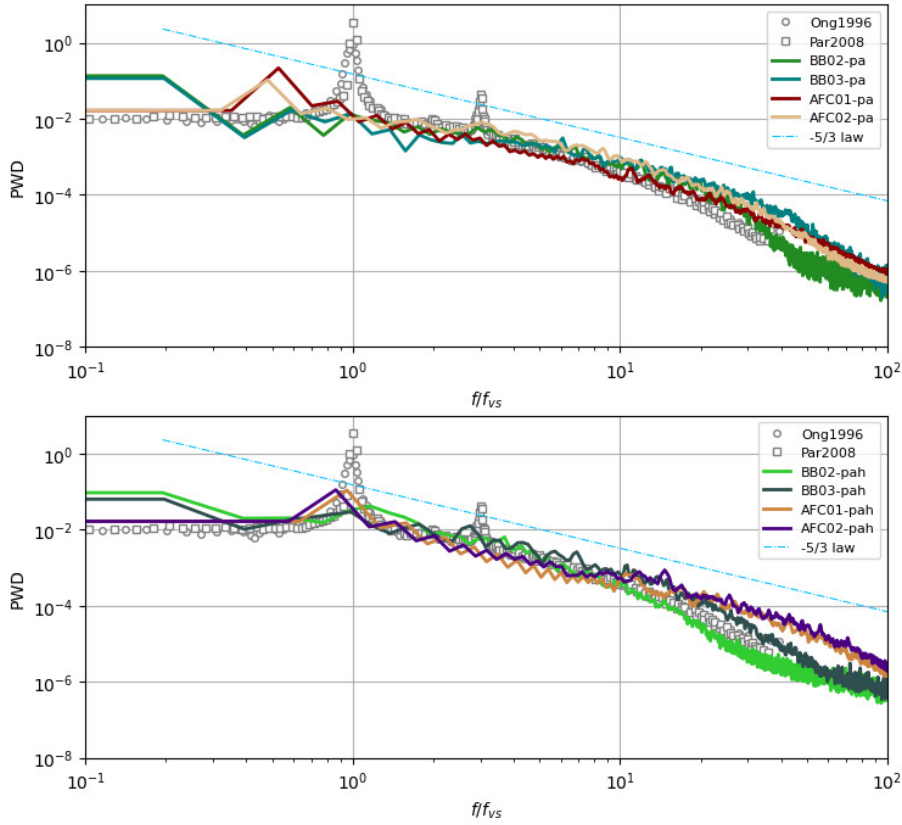

Figure 10: One-dimensional spectra of the transverse velocity in the vicinity of the bluff-body without trapped vortex cells and with integrated AFC obtained at the downstream location $x/D = 1$, $z/D = 0$ (a) and $x/D = 1$, $z/D = 0.25$ (b)

The Strouhal numbers of the vortex shedding frequency computed for BB were $St_p \approx 0.32$, based on the FFT analysis. It was interesting that the dominant frequency was pronounced well for all velocity components, as shown in Fig. 11,a, where results of the continued wavelet transform (CWT) are plotted.

The CWT analysis was performed using the same mathematical apparatus described by Lysenko et al. [19]. The computed Strouhal numbers were slightly less compared to the values obtained for HC1, HC2 ($\text{St}_p = 0.371 - 0.396$). These results could be explained by effects of superposition of oscillations from the primary detached separated bubble and the pair of vortex structures generated from the semi-spheres of the bluff-body. From the experimental point of view, Yamagata et al. [14] obtained $\text{St}_p = 0.37$. This significantly underestimated measurements by Isaev et al. [16], who predicted $\text{St}_p = 0.41 - 0.44$. It was noted that the pressure coefficient signals were used by Isaev et al. [16] to obtain experimental values. As a result, it was somewhat unusual, since most experimental St have been obtained from the lift coefficient or velocity time series. The chamfered edges of HC may be another possible explanation of the results discussed in Sect. 5.2.1. According to Carassale et al. [51], some decrease was likely in this case as well, due to the close relationship between the Strouhal number and the lift force.

5.3. Effect of the active flow control based on the trapped vortex cells

The integral flow parameters are provided in Table 3 and Fig. 8. Figure 7,c shows that the massive, detached recirculation zone over the obstacle with AFC had mostly vanished, resulting in the positive mean lift coefficient $\langle C_l \rangle = 0.75 - 0.76$. Axial distributions of the mean stream-wise velocity and its fluctuations shown in Fig. 8 supported these findings. The small separated bubble still existed near the trailing edge and was characterized by the recirculation length $\langle L_d/D \rangle = 0.09 - 0.102$. The total, mean drag coefficient was calculated as $\langle C_d \rangle = 0.51 - 0.52$, indicating that the implemented AFC contributed additional energy losses of about 10% in terms of the drag coefficient. Finally, in spite of existence of the recirculation zone attached to the pressure side of the obstacle and two lateral vortex structures originated from the lateral surfaces of the obstacle, its aerodynamic performance was improved significantly. The calculated aerodynamic quality, defined as the lift-to-drag coefficients ratio, of the obstacle with AFC was $K = C_l/C_d = 1.47$, compared to BB without AFC
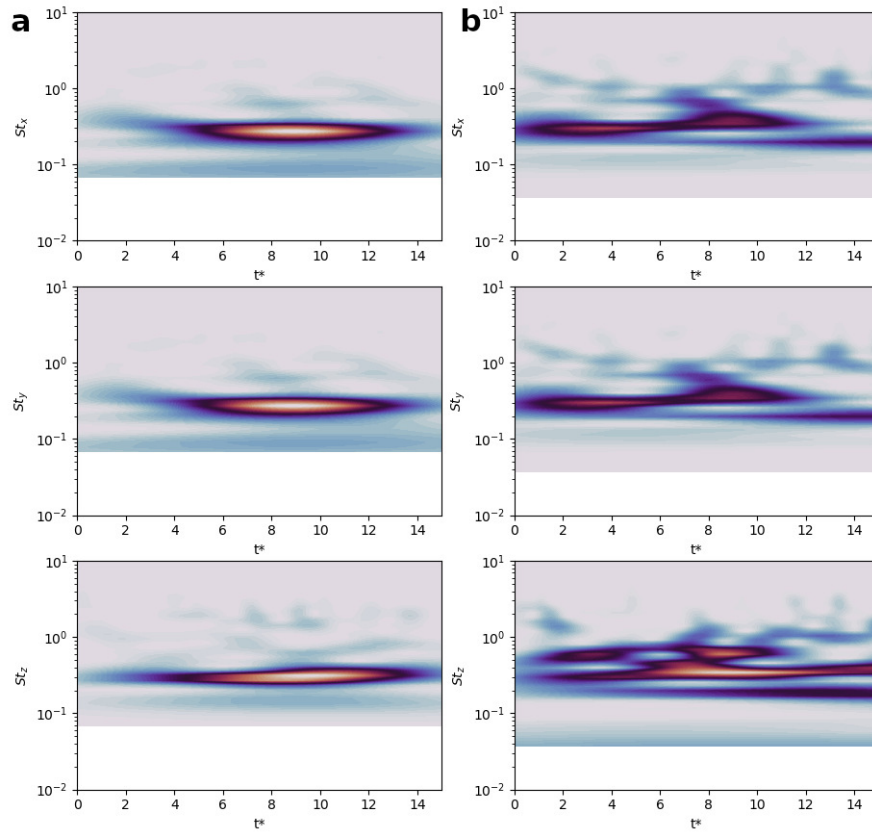
Figure 11: Wavelet energy density maps calculated for BB02 (a) and BB-AFC02 (b) at the downstream location $x/D = 1$, $z/D = 0$: 70 filled iso-contours from 0 to 1

of $K = -0.9$.

It is interesting to compare the instantaneous flow visualization obtained for the vehicle with and without AFC, as well. Figures 9,b,c and 12,a,b compare the instantaneous flow visualization in terms of iso-surfaces of the Q-criterion obtained for the vehicle with and without AFC displayed from the frontal and top views. It was noted that the direction of the downstream wake convection was different for the bluff-body with and without AFC, due to the positive and negative lift force. Spectral results are provided in Figs. 10 and 11. One-dimensional spectra calculated for AFC01 and AFC02 collapsed well to the similar data obtained for BB01 and BB02, indicating that a large part of the inertial sub-range was resolved reasonably well in the present LES. This finding is confirmed in Figs. 9,b,c and 12,a,b, where the coherent energetic structures of different scales are displayed. Finally, Fig. 11,b presents results of continued wavelet transform (CWT) calculated for the velocity signals sampled at the downstream wake location ($x/D = 1$, $z/D = 0$). It is worth mentioning that the presented CWT in Fig. 11,b contains superposition of the energy patterns, which related to the two trapped vortex cells and remained attached and detached recirculation zones.

6. Discussion

It is important to note that the numerical platform used in the present simulations was tested intensively during the last decade and highly recommended itself as sufficiently accurate and efficient tool to simulate the turbulent separated flows [18], [19], [27], [28], [29], [20], [30], [21], [12]. Thus, with some level of confidence, we think that the present numerical results can be used to prove the initial concept in the lack of experimental data.

The location of the two vortex cells at the suction side of the BB at the zero angle of attack led to a radical transformation of the quasi-steady flow over the obstacle, where the separation zone was mostly vanished, and the wake dynamics was completely suppressed. At the same time, the drag and
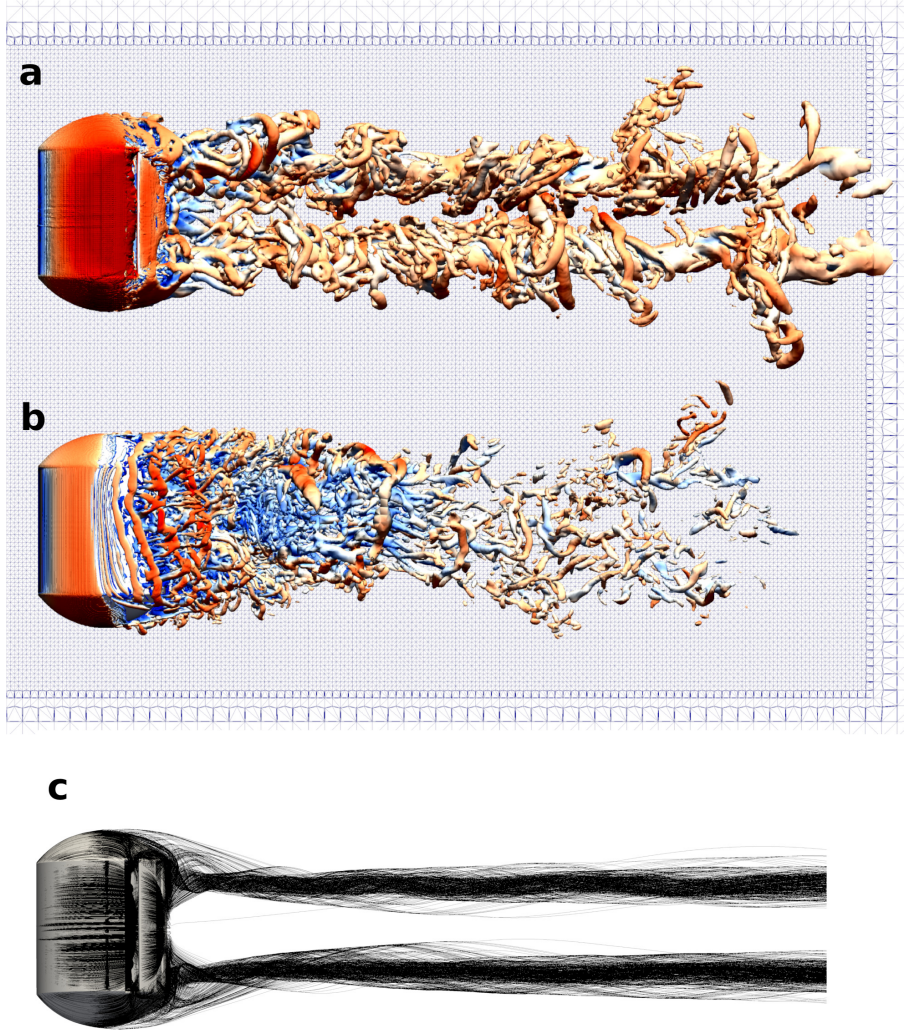
29

Figure 12: Visualization of the flow structures obtained for the flow past the bluff-body with the integrated active control system (a) and without trapped vortex cells (b). Iso-surfaces of the Q-criterion ($Q = S^2 - \Omega^2 = 10^4$, where S is the strain rate and Ω is the vorticity). Time-averaged streamlines for the flow over the vehicle with AFC (c)
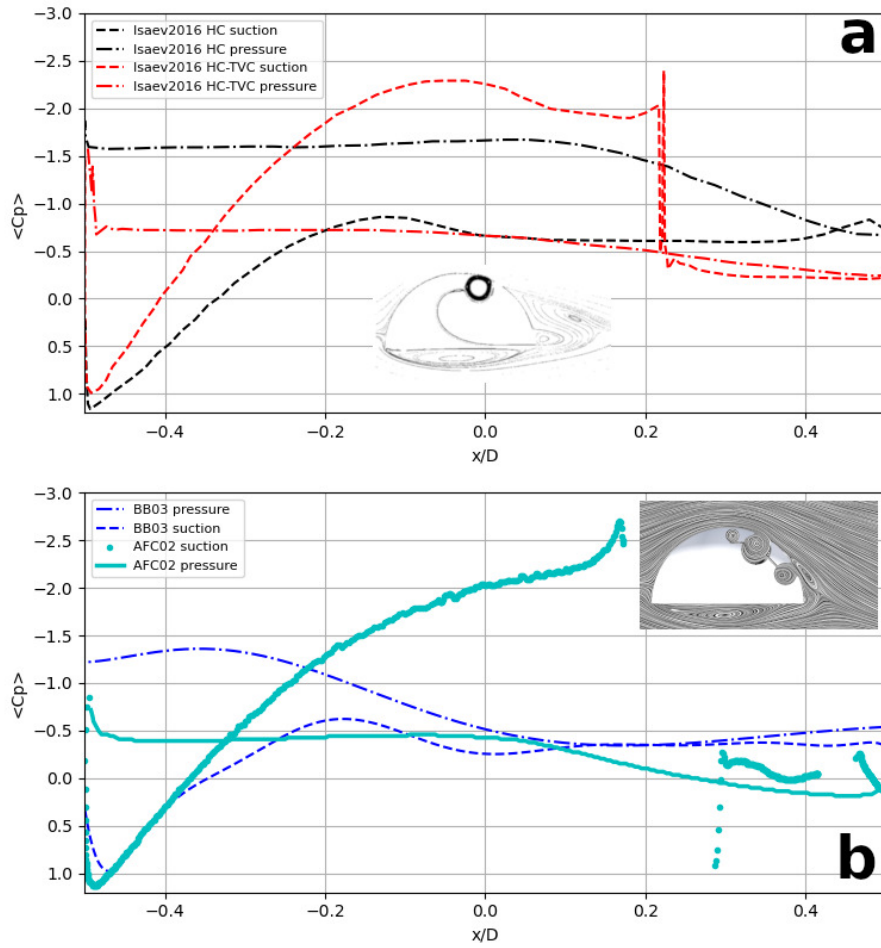
30

Figure 13: Distribution of the mean pressure coefficient over the suction and pressure sides of the two-dimensional semi-circular cylinder with one TVC (a) [11] and BB with two TVCs (b) along the chord (AFC02) as well as $\langle C_p \rangle$ profiles obtained for the obstacles without vortex cells (HC and BB03, respectively)

31

lift forces changed drastically. The BB, based on the semi-circular profile, is characterized by the low negative lift coefficient $\langle C_l \rangle \sim -0.5$. When the AFC system was placed, the lift force became positive $\langle C_l \rangle \sim 0.75$, coupled with the small increase ($\approx 10\%$) of the total drag coefficient caused by the energy losses of the flow control system.

Analyzing the present results with calculations reported by Isaev [11] for the two-dimensional semi-circular cylinder with one integrated trapped vortex cell was interesting from a numerical point of view. Isaev [11] used the classical Reynolds-averaged Navier-Stokes approach at a similar Reynolds number and zero angle of attack. Figure 13,a presents profiles of the mean pressure coefficient over the suction and pressure sides of HC with and without TVC. Distribution of the pressure coefficient computed for BB and AFC with two TVCs is displayed in Fig. 13,b. Qualitative similarity between configurations with one and two TVCs can be observed: implementation of the vortex cells on the suction side of the airfoil led to a significant restructuring of the distribution of the local pressure along its cord. At the upper side of the vehicle, the static pressure decreased several times up to location of the first vortex cell, whereas behind TVC, the pressure became higher than for the base profile. The static pressure increased on the pressure side of the airfoils, as well, when TVC was placed. As a result, the negative lift changed its sign to positive. Quantitatively, Isaev [11] predicted the aerodynamic quality as, $K = 2.22$ for HC with TVC and $K = -2.04$ for the smooth HC without the vortex cell. The present results revealed $K = 1.5$ for the vehicle with two TVCs and $K = -0.9$ for the case without vortex cells.

7. Concluding remarks

The novel bluff-body design with the active flow control system based on the trapped vortex cells was presented and accompanied by the pioneering numerical investigation using the large-eddy simulations. The present concept allows significant suppression of vortex shedding in bluff-body flows, which can

be used in various ocean engineering and marine science applications. Here, we see the two main classes for potential usage. The first group is dedicated to novel autonomous aerial and underwater vehicles for transportation, inspection, monitoring and observation purposes. In the second group are various scenarios, where the bluff-body wake control is needed, seem as alternative for practical implementations (vortex-induced vibrations problems, heat transfer technologies, construction of buildings and city landscapes, etc.).

The LES technique was used to compute the flow past the bluff-body without and with active flow control at zero angle of attack and Re = 50000 as the consistent continuation of the previous study for the semi-circular cylinder [12]. The active flow control system with the slot fluid suction was based on the two trapped vortex cells distributed on the suction side of the obstacle. The implemented active flow control system (with some level of abstraction) successfully demonstrated the nearly undetached flow past the bluff-body. The aerodynamic performance (the lift-to-drag ratio) of the obstacle with active flow control was improved significantly to $K = 1.5$. This compares to the original bluff-body without AFC, which has a negative lift force and $K = -0.9$. The energy losses of the AFC system was estimated of approximately 10% in terms of the total drag force.

The next steps of the research will be in the further system advancing to minimize the remaining parasitic separated zone and vortex structures from the lower and lateral sides of the obstacle and decrease the system energy losses. Optimization of amount of the trapped vortex cells and their location also seems necessary. Additionally, it will be interesting to apply the stability theory to investigate the sensitivity of AFC on the inlet turbulence intensity and the angle of attack. The compressible and viscous effects (increasing Mach and Reynolds numbers) are of interest as well.

References

[1] D. Greenblatt, D. Williams, Flow control for Unmanned Air Vehicles, Annual Review Fluid Mech. 54 (2022) 383–412.

[2] S. Rashidi, M. Hayatdavoodi, J. Esfahani, Vortex shedding suppression and wake control: a review, Ocean Eng. 126 (2016) 57–80.

[3] W.-L. Chen, Y. Huang, C. Chen, H. Yu, D. Gao, Review of active control of circular cylinder flow, Ocean Eng. 258 (2022) 111840.

[4] J. Derakhshandeh, M. M. Alam, A review of bluff body wakes, Ocean Eng. 182 (2019) 475–488.

[5] M. Lekkala, M. Latheef, J. Jung, A. Coraddu, H. Zhu, N. Srinil, B.-H. Lee, D. Kim, Recent advances in understanding the flow over bluff bodies with different geometries at moderate Reynolds numbers, Ocean Eng. 261 (2022) 111611.

[6] S. Sedda, C. Sardu, D. Lasagna, G. Iuso, R. S. Donelli, F. D. Gregorio, Trapped vortex cell for aeronautical applications: flow analysis through PIV and Wavelet transform tools, in: 10th Pacific Symposium on Flow Visualization and Image Processing, Naples, Italy, 2015.

[7] F. O. Ringleb, Separation control by trapped vortices. in: Boundary layer and flow control, Ed. Lachmann G.V., Pergamon Press (1961).

[8] W. Kasper, Aircraft wing with vortex generation, US Patent No. 3831885 (1974).

[9] A. I. Savitsky, L. N. Schukin, V. G. Karelin, A. M. Mass, R. M. Pushkin, A. P. Shibamov, I. L. Schukin, S. V. Fischenko, Method for controlling boundary layer on an aerodynamic surface of a flying vehicle, US Patent No. 5417391 (1995).

[10] A. V. Ermishin, S. A. Isaev, Flow control past bodies with vortex cells applied to a blended wing-body aircraft (numerical and physical modeling)(In Russian), St.Petersburg University of Civil Aviation, Saint-Petersburg, Moscow (2001).

[11] S. A. Isaev, Aerodynamics of thickened bodies with vortex vells (numerical and physical modeling)(In Russian), St.Petersburg Polytechnic University, Saint-Petersburg (2016).

[12] D. A. Lysenko, I. S. Ertesvåg, Large-eddy simulations of the flow over a semi-circular cylinder at Re = 50000, Comput. Fluids 228 (2021) 105054.

[13] Z. P. Sluchanovskaya, Pressure distribution on the surface of rectangular, trihedral, and semicircular cylinders and their aerodynamic coefficients (in Russian), Nauchn. Tr. Inst. Mekh. 24 (1973) 52–60.

[14] T. Yamagata, N. Saito, N. Fujisawa, Aeolian tone from a semi-circular cylinder in a stream, J. Flow Control, Measurement Visualization 4 (2016) 30–37.

[15] S. A. Isaev, P. A. Baranov, A. G. Sudakov, I. A. Popov, A. E. Usachov, Controlling the flow past a semicircular airfoil at zero angle of attack using slot suction in one or two vortex cells for attaining external lift, Technical Physics Letters 43(12) (2017) 1115–1117.

[16] S. Isaev, P. Baranov, I. Popov, A. Sudakov, A. Usachov, S. Guvernyuk, A. Sinyavin, A. Chylunin, A. Mazo, E. Kalinin, Ensuring safe descend of reusable rocket stages - Numerical simulation and experiments on subsonic turbulent air flow around a semi-circular cylinder at zero angle of attack and moderate Reynolds number, Acta Astronautica 150 (2018) 117–136.

[17] S. Isaev, P. Baranov, I. Popov, A. Sudakov, A. Usachov, S. Guvernyuk, A. Sinyavin, A. Chylunin, A. Mazo, D. Demidov, A. Dekterev, A. Gavrilov, A. Shebelev, Numerical simulation and experiments on turbulent air flow around the semi-circular profile at zero angle of attack and moderate Reynolds number, Comput. Fluids 188 (2019) 1–17.

[18] D. A. Lysenko, I. S. Ertesvåg, K. E. Rian, Large-eddy simulation of the flow over a circular cylinder at Reynolds number 3900 using the OpenFOAM toolbox, Flow Turbul. Combust. 89 (2012) 491–518.

[19] D. A. Lysenko, I. S. Ertesvåg, K. E. Rian, Large-eddy simulation of the flow over a circular cylinder at Reynolds number 2×10^4, Flow Turbul. Combust. 92 (2014) 673–698.

[20] D. A. Lysenko, I. S. Ertesvåg, Reynolds-averaged, scale-adaptive and large-eddy simulations of premixed bluff-body combustion using the Eddy Dissipation Concept, Flow Turbul. Combust. 100 (2018) 721–768.

[21] D. A. Lysenko, I. S. Ertesvåg, Assessment of algebraic subgrid scale models for the flow over a triangular cylinder at Re = 45000, Ocean Engin. 222 (2021) 108559.

[22] B. Geurts, Elements of Direct and Large-Eddy Simulation, R.T.Edwards, Philadelphia (2004).

[23] A. Yoshizawa, Statistical theory for compressible shear flows, with the application to subgrid modelling, Phys. Fluids 29(2152) (1986) 1416–1429.

[24] P. Sagaut, Large Eddy Simulation for Incompressible Flows, 3rd ed., Springer Berlin (2006).

[25] H. G. Weller, G. Tabor, H. Jasak, C. Fureby, A tensorial approach to computational continuum mechanics using object-oriented techniques, Comp. Phys. 12(6) (1998) 620–631.

[26] M. Prsic, M. Ong, B. Pettersen, D. Myrhaug, Large Eddy Simulations of flow around a smooth circular cylinder in a uniform current in the subcritical flow regime, Ocean Eng. 77 (2014) 61–73.

[27] Y. Cao, T. Tamura, Numerical investigations into effects of three-dimensional wake patterns on unsteady aerodynamics characteristics of a circular cylinder at Re= 1.3×10^5, J. Fluids Struct. 59 (2015) 351–369.

[28] E. Robertson, V. Choudhury, S. Bhushana, D. K. Walters, Validation of OpenFOAM numerical methods and turbulence models for incompressible bluff body flows, Comput. Fluids 123 (2015) 122–145.

[29] Y. Cao, T. Tamura, Large-eddy simulations of flow past a square cylinder using structured and unstructured grids, Comput. Fluids 137 (2016) 36–54.

[30] A.-P. Zahiri, E. Roohi, Anisotropic minimum-dissipation (AMD) subgrid-scale model implemented in OpenFOAM: Verification and assessment in single-phase and multi-phase flows, Comput. Fluids 180 (2019) 190–205.

[31] Y. Jin, Z. Cheng, X. Han, J. Mao, F. Jin, VLES of drag reduction for high Reynolds number flow past a square cylinder based on OpenFOAM, Ocean Eng. 190 (2019) 106450.

[32] D. A. Lysenko, I. S. Ertesvåg, K. E. Rian, Modeling of turbulent separated flows using OpenFOAM, Comput. Fluids 80 (2013) 408–422.

[33] J. P. Vandoormaal, G. D. Raithby, Enhancements of the SIMPLE method for predicting incompressible fluid flows, Numer. Heat Transfer 7 (1984) 147–163.

[34] H. Weller, Controlling the computational modes of the arbitrarily structured C grid, Monthly Weather Rev. 140(10) (2012) 3220–3234.

[35] A. Harten, High resolution schemes for hyperbolic conservation laws, J. Comput. Phys. 49 (1983) 357–393.

[36] C. H. K. Williamson, J. Wu, J. Sheridan, Scaling of streamwise vortices in wakes, Physics Fluids 7(10) (1995) 2307–2309.

[37] Y. Cao, T. Tamura, H. Kawai, Spanwise resolution requirements for the simulation of high-Reynolds-number flows past a square cylinder, Comput. Fluids 196 (2020) 104320.

[38] D. A. Lysenko, I. S. Ertesvåg, K. E. Rian, Numerical simulations of the Sandia flame D using the Eddy Dissipation Concept, Flow Turbul. Combust. 93 (2014) 665–687.

[39] J. Son, T. Hanratty, Velocity gradients at the wall for flow around a cylinder at Reynolds numbers from 5×10^3 to 10^5, J. Fluid Mech. 35 (1969) 353–368.

[40] A. Perry, W. Schofield, P. Joubert, Rough wall turbulent boundary layers, J. Fluid Mech. 37(2) (1969) 383–413.

[41] A. A. McKillop, F. Durst, A laser anemometry study of separated flow behind a circular cylinder, In Laser anemometry in fluid mechanics II (ed. R. J. Adrian, et al.) LADOAN-IST, Lisbon, Portugal (1986).

[42] H. C. Lim, S. J. Lee, Flow control of circular cylinders with longitudinal grooved surfaces, AIAA J. 40(10) (2002) 2027–2036.

[43] D. F. G. Durao, M. V. Heitor, J. C. F. Pereira, A laser anemometry study of separated flow around a squared obstacle, In Laser anemometry in fluid mechanics II (ed. R. J. Adrian, et al.) LADOAN-IST, Lisbon, Portugal (1986).

[44] D. Lyn, S. Einav, W. Rodi, J. Park, A laser doppler velocimetry study of ensemble-averaged characteristics of the turbulent near wake of a square cylinder, J. Fluid Mech. 304 (1995) 285–319.

[45] S. Sanquer, P. Bruel, B. Deshaies, Some specific characteristics of turbulence in the reactive wakes of bluff bodies, AIAA J. 36(6) (1998) 994–1001.

[46] M. Minguez, C. Brun, R. Pasquetti, E. Serre, Experimental and high-order LES analysis of the flow in near-wall region of a square cylinder, Int. J. Heat Fluid Flow 32 (2011) 558–566.

[47] F. X. Trias, A. Gorobets, A. Oliva, Turbulent flow around a square cylinder at Reynolds number 22,000: A DNS study, Comput. Fluids 123 (2015) 87–98.

[48] P. Welch, The use of fast Fourier transform for the estimation of power spectra: a method based on time averaging over short, modified periodograms, IEEE Trans. Audio Electroacoust. 15(6) (1967) 70–73.

[49] L. Ong, J. Wallace, The velocity field of the turbulent very near wake of a circular cylinder, Exp. Fluids. 20 (1996) 441–453.

[50] P. Parnaudeau, J. Carlier, D. Heitz, E. Lamballais, Experimental and numerical studies of the flow over a circular cylinder at Reynolds number 3900, Phys. Fluids 20 (2008) 085101.

[51] L. Carassale, A. Freda, M. Marrè-Brunenghi, Experimental investigation on the aerodynamic behavior of square cylinders with rounded corners, J. Fluids Structures 44 (2014) 195–204.